

Banner appropriate to article type will appear here in typeset article

# 1 Transition to turbulence in wind-drift layers

2 **Gregory LeClaire Wagner,<sup>a</sup>† Nick Pizzo,<sup>b,c</sup> Luc Lenain,<sup>c</sup> Fabrice Veron<sup>d</sup>**

3 <sup>a</sup>Massachusetts Institute of Technology

4 <sup>b</sup>University of Rhode Island Graduate School of Oceanography

5 <sup>c</sup>Scripps Institution of Oceanography, University of California, San Diego

6 <sup>d</sup>University of Delaware

7 (Received xx; revised xx; accepted xx)

8 A light breeze rising over calm water initiates an intricate chain of events that culminates  
9 in a centimeters-deep turbulent shear layer capped by gravity-capillary ripples. At first,  
10 viscous stress accelerates a laminar wind-drift layer until small surface ripples appear. The  
11 surface ripples then catalyze the growth of a second instability in the wind-drift layer,  
12 which eventually sharpens into along-wind jets and downwelling plumes, before devolving  
13 into three-dimensional turbulence. This paper elucidates the evolution of wind-drift layers  
14 after ripple inception using wave-averaged numerical simulations with a constant-amplitude  
15 representation of the incipient surface ripples. The simulations reproduce qualitative aspects  
16 of laboratory experimental measurements of the phenomena, thereby validating the wave-  
17 averaged numerical approach. But we also find that our results are disturbingly sensitive to the  
18 amplitude of the prescribed surface wave field, raising the question whether wave-averaged  
19 models are truly “predictive” if they do not also describe the coupled evolution of the surface  
20 waves together with the flow beneath.

## 21 1. Introduction

22 The appearance of surface ripples beneath gusts of wind is an everyday experience on the  
23 water, belying a surprisingly intricate chain of events unfolding beneath the surface. There, an  
24 accelerating wind-drift layer breeds two instabilities in sequence: first the surface instability  
25 that generates ripples, followed by a subsurface instability whose growth, finite amplitude  
26 saturation, and destabilization to three-dimensional perturbations ultimately gives way to  
27 persistent turbulence in the centimeters-thick wind-drift layer.

28 This ubiquitous transition-to-turbulence scenario was observed in a series of laboratory  
29 experiments reported by Melville *et al.* (1998), Veron & Melville (1999) and Veron &  
30 Melville (2001), who subjected an initially quiescent wave tank to a turbulent airflow rapidly  
31 accelerated from rest to a constant airspeed. One of Veron & Melville (2001)’s key results  
32 is that both the generation of surface ripples and the transition to turbulence are suppressed  
33 by surfactant layered on the water surface. This surfactant experiment proves that ripples are  
34 intrinsic to the second slow instability implicated in the turbulent transition of the wind-drift  
35 layer under typical conditions (disproving Handler *et al.* (2001)’s hypothesis, repeated by  
36 Thorpe (2004), that the transition to turbulence is convective).

† Gregory Wagner, gregory.leclaire.wagner@gmail.com

Motivated by Veron & Melville (2001)'s experimental results, we propose a wave-averaged model based on the "Craik-Leibovich" (CL) Navier-Stokes equations (Craik & Leibovich 1976) for the development of wind-drift layers — eventually leading to a transition to turbulence — after the appearance of capillary ripples. We focus narrowly on a comparison with a new laboratory experiment similar to those reported by Veron & Melville (2001) and described in section 2. The predictions of our wave-averaged model are developed in section 3. We combine analytical results from Veron & Melville (2001) on the initial laminar developments with a linear instability analysis of the wind-drift layer just after ripple inception, and with numerical simulations of nonlinear development of the second slow instability from ripple inception to fully developed wind-drift turbulence.

We have two goals: first, we seek a more detailed understanding of the wind-drifted transition to turbulence. Second, we seek to validate the wave-averaged Craik-Leibovich (CL) momentum equation, which is central to parameterization of ocean surface boundary layer turbulence (see for example D'Asaro *et al.* 2014; Harcourt 2015; Reichl & Li 2019). Toward this second goal we make some progress and find that our CL-based model qualitatively replicates the laboratory measurements — most strikingly during the transition to turbulence depicted in figure 5. Yet we also find our results are delicately sensitive to the parameters of the prescribed ripples, which owing to uncertainty about the evolving, two-dimensional state of the ripples surrounding the transition to the turbulence, prevents unambiguous conclusions about CL validity. In section 4, we discuss how that this sensitivity suggests that CL is "incomplete" because it does not also predict the *response* of the wave field to the currents and turbulence beneath.

## 2. Laboratory experiments of winds rising over calm water

This paper uses an experiment similar to those reported by Melville *et al.* (1998) and Veron & Melville (2001). The experiments were conducted in the 42-m long, 1-m wide, 1.25-m high wind-wave-current tank at the Air-Sea Interaction Laboratory of the University of Delaware, and used a computer-controlled recirculating wind tunnel to accelerate a turbulent airflow to  $10 \text{ m s}^{-1}$  over 65 s. The water depth was maintained at 0.71 m and observations were collected at a fetch of 12 m. An artificial wave-absorbing beach dissipated wave energy and eliminated wave reflections at the downwind end of the tank. A schematic of the experimental setup is shown in figure 1.

### 2.1. Laser-induced fluorescence (LIF) observations

The evolution of initially surface-concentrated dye was observed with a Laser-Induced Fluorescence (LIF) system. Images were acquired with a CCD camera (Jai TM4200CL, 2048 × 2048 pixels) equipped with an 85 mm Canon EF lens focused at the air-water interface. Illumination was provided by a thin 3 mm thick laser light sheet generated by a pulsed dual-head Nd-Yag laser (New Wave Research, 120 mJ/pulse, 3–5 ns pulse duration). The laser light sheet illuminated a thin layer of fluorescent dye carefully applied to the water surface prior to each experiment. Observations were conducted with the vertical light sheet in both along-wind and transverse directions. The LIF camera collected images at a 7.2 Hz frame rate and with a field of view of 11.6 x 11.6 cm in the along-wind configuration, and 13.9 x 13.9 cm in the transverse direction.

### 2.2. Surface wave observations

The evolution of the surface wave profiles were collected using a separate CCD camera (Jai TM4200CL, 2048 × 2048 pixels) equipped with an 60 mm Nikor lens focused at the air-water

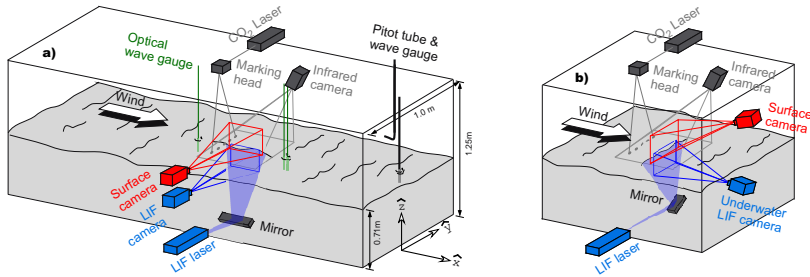


Figure 1: Schematic of the wind-wave-current tank at the Air-Sea Interaction Laboratory of the University of Delaware at a fetch of 12 m, showing (a) the along-wind section imaged by Laser Induced Fluorescence (LIF) and (b) the cross-wind LIF setup.

82 interface. This camera made use of the LIF illumination system and was synchronized with  
 83 the LIF camera. As with the LIF images, surface profiles images were collected in both  
 84 along-wind and transverse directions with a field of view of 20.1 cm x 20.4 cm and 24.5 cm  
 85 x 25 cm respectively. Surface wave elevation profiles were extracted from the images using  
 86 an edge detection algorithm based on local variations of image intensity gradients and which  
 87 used kernel convolution to identify the location of the surface in the LIF images (see Buckley  
 88 & Veron 2017 for details).

89 In addition, the waves were measured using optical wave gauges made of 200 mW CW  
 90 green lasers (2 mm beam diameter) and CCD cameras (Jai CV-M2, 1600 x 120 pixels).  
 91 A single wave gauge was positioned 2 cm upstream of the LIF field of view; the camera  
 92 was equipped with a 180 mm Nikon lens which resulted in a 19.4  $\mu\text{m}$  per pixel resolution.  
 93 A double wave gauge with two adjacent lasers, separated by 1.4 cm, was placed 3 cm  
 94 downstream of the LIF field of view. There, the camera was equipped with a 60 mm Nikon  
 95 lens which resulted in a 66.4  $\mu\text{m}$  per pixel resolution. At both locations, single-point elevation  
 96 measurements were obtained at 93.6 Hz.

### 97 2.3. Thermal Marking Velocimetry (TMV)

98 In addition to LIF, we employed Thermal Marking Velocimetry (TMV), as developed by  
 99 Veron & Melville (2001) and Veron *et al.* (2008), to measure the surface velocity by tracking  
 100 laser-generated Lagrangian heat markers in thermal imagery of water surfaces. In the present  
 101 experiment, infrared images of the surface were captured by a 14-bit, 640 x 512 quantum  
 102 well infrared photodetector (QWIP, 8.0–9.2  $\mu\text{m}$ ) FLIR SC6000 infrared camera operated at  
 103 a 43.2 Hz frame rate, with an integration time of 10 ms, and a stated rms noise level below  
 104 35 mK. After image correction to account for the slightly off-vertical viewing angle of the  
 105 imager, the resulting image sizes were 24.6 cm x 24.6 cm.

106 The infrared imager is sensitive enough to detect minute, turbulent temperature variations  
 107 in the surface thermal skin layer (Jessup *et al.* 1997; Zappa *et al.* 2001; Veron & Melville  
 108 2001; Sutherland & Melville 2013). It thus easily detects active weakly-heated markers,  
 109 generated by a 60 W air-cooled CO<sub>2</sub> laser (Synrad Firestar T60) equipped with an industrial  
 110 marking head (Synrad FH Index) and two servo-controlled scanning mirrors programmed to  
 111 lay down a pattern of 16 spots with 0.8 cm diameter and at a frequency of 1.8 Hz.

112 The spatially averaged surface velocity was estimated by tracking the geometric centroid  
 113 of these Lagrangian heat markers for approximately 1 s. Both Gaussian interpolation (which  
 114 has sub-pixel resolution due to the Gaussian pattern of the laser beam) and a standard  
 115 cross-correlation technique yielded similar estimates for the surface velocity.

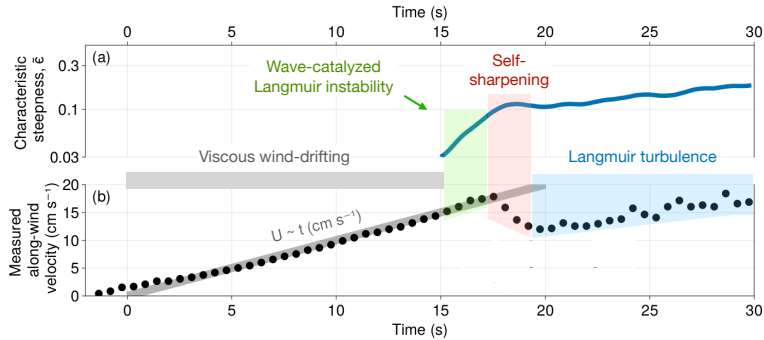


Figure 2: Summary of laboratory measurements: (a) an estimate of the characteristic along-wind steepness of the surface wave field obtained from the surface wave profile measurements; (b) the average along-wind surface velocity measured with the thermal marking velocimetry technique.

116

#### 2.4. Summary of experimental results

117 Figure 2 summarizes the experimental results. Figure 2a shows a time series of the  
 118 characteristic along-wind wave steepness (Melville *et al.* 1998),

$$119 \quad \tilde{\epsilon}(t) \equiv \sqrt{2 \overline{\eta_x^2}}, \quad (2.1)$$

120 where  $\eta(x, t)$  is the surface displacement measured by the surface imaging camera,  $\eta_x(x, t)$   
 121 is the  $x$ -derivative of  $\eta$ , and the overline  $(\cdot)$  denotes an  $x$  average over the along-wind field  
 122 of view of the surface imaging camera. Figure 2b shows the measured average along-wind  
 123 surface velocity using TMV. The thick gray line in figure 2b plots  $A t$ , where  $A = 1 \text{ cm s}^{-2}$   
 124 showing that the surface current increases linearly, at least initially. (The time axis for  
 125 laboratory measurements is adjusted to meet this line, which constitutes a definition of  
 126 “ $t = 0$ ”.) Following Veron & Melville (2001), figures 2a–b divide the development of the  
 127 waves and currents into four stages:

128 (i) *Viscous acceleration*,  $t = 0$ –16 s. In the first stage, viscous stress between the  
 129 accelerating wind and water accelerates a shallow, laminar, viscous wind-drift layer.

130 (ii) *Wave-catalyzed “Langmuir” shear instability*,  $t = 16$ –18 s. At  $t \approx 16$  s, detectable  
 131 capillary ripples appear. A wave-catalyzed shear instability — which obey the same dynamics  
 132 as “Langmuir circulation”, which often refers to much larger scale motions in the ocean  
 133 surface boundary layer Craik & Leibovich (1976) — immediately starts to develop and grow  
 134 in the wind-drift layer.

135 (iii) *Self-sharpening*,  $t = 18$ –20 s. When the shear instability reaches finite amplitude,  
 136 nonlinear amplification due to perturbation self-advection sharpens the instability features  
 137 into narrow jets and downwelling plumes.

138 (iv) *Langmuir turbulence*,  $t > 20$  s. The self-sharpened circulations develop significant  
 139 three-dimensional characteristics and transition to fully developed Langmuir turbulence.

140 **3. A wave-averaged model for the transition to turbulence in wind-drift layers**

141 The main purpose of this paper is to build a model for the four-stage evolution of the wind-  
 142 drift layer in the water, focusing on the dynamics after the inception of surface capillary  
 143 ripples.

### 3.1. Viscous acceleration

145 As the wind starts to accelerate, viscous stress across the air-water interface drives a laminar  
146 wind-drift current in the water. The thick gray line in figure 2 indicates that the average  
147 velocity at the water surface nearly obeys

$$U(z=0, t) \equiv U_0(t) = A t, \quad (3.1)$$

149 where  $A \approx 1 \text{ cm s}^{-2}$ . Veron & Melville (2001) point out that the viscous stress consistent  
 150 with linear surface current acceleration is

$$\tau(t) = \alpha\sqrt{t}\hat{x} \quad (3.2)$$

where  $\tau$  is the downwards kinematic stress across the air-water interface,  $\hat{x}$  is the along-wind direction ( $\hat{y}$  and  $\hat{z}$  are the cross-wind and vertical directions), and  $\alpha \approx 0.12 \text{ cm}^2 \text{ s}^{-5/2}$  produces  $A = \alpha \sqrt{4/\pi\nu} \approx 1 \text{ cm s}^{-2}$  given the kinematic viscosity of water,  $\nu = 0.011 \text{ cm}^2 \text{ s}^{-1}$ . The laminar, viscous wind-drift shear layer in the water forced by (3.2) takes the form (Veron & Melville 2001)

$$157 \quad U(z, t) = U_0(t) \left[ \left(1 + \delta^2\right) \operatorname{erfc}\left(-\frac{\sqrt{2}}{2} \delta\right) + \delta \sqrt{\frac{2}{\pi}} \exp\left(-\frac{1}{2} \delta^2\right) \right], \quad \text{where} \quad \delta \equiv \frac{z}{\sqrt{2}vt}. \quad (3.3)$$

158 Viscous acceleration continues until gravity-capillary ripples appear at the air-water interface  
 159 when  $t \approx \tilde{t} \equiv 16$  s and thus  $U_0(t) \approx \tilde{U}_0 \equiv 16$  cm s<sup>-1</sup>.

### 3.2. Instability of the wind-drift layer catalyzed by incipient capillary ripples

161 As soon as ripples appear on the water surface, a second, slower, non-propagating instability  
162 begins to grow within the wind-drift layer in the water. Remarkably, this second instability  
163 is catalyzed by and therefore requires the presence of capillary ripples: for example Veron  
164 & Melville (2001) show that instability and turbulence are suppressed if ripple generation is  
165 inhibited by layering surfactant on the water surface.

To describe the development of the wind-drift layer modified by the appearance of capillary ripples, we use the wave-averaged “Craik-Leibovich” (CL) momentum equation. In the CL momentum equation, the surface wave field is prescribed, which means that wave generation cannot be described. The formal validity of the CL momentum equation requires that the ripples are not too steep. Figure 2a plots an estimate of the characteristic wave steepness  $\tilde{\epsilon}(t)$  defined by equation (2.1), showing that by the time ripples reach detectable amplitudes they have small slopes with  $\tilde{\epsilon} = 0.1$ . We thus expect that the CL momentum equation can at least describe the initial development of the instability that follows ripple inception.

The wave-averaged Craik-Leibovich equation (Craik & Leibovich 1976) formulated in terms of the Lagrangian-mean momentum  $\mathbf{u}^L$  of the wind-drift layer is

$$\boldsymbol{u}_t^L + (\boldsymbol{u}^L \cdot \nabla) \boldsymbol{u}^L - (\nabla \times \boldsymbol{u}^S) \times \boldsymbol{u}^L + \nabla p^E = \nu \Delta \boldsymbol{u}^L - \nu \Delta \boldsymbol{u}^S + \boldsymbol{u}_t^S, \quad (3.4)$$

where  $\mathbf{u}^S$  is the Stokes drift of the field of capillary ripples and  $p^E$  is the Eulerian-mean pressure. The asymptotic derivation of the CL equation (3.4) requires  $\epsilon \ll 1$ . We require  $\mathbf{u}^L$  to be divergence-free (Vanneste & Young 2022),

$$\nabla \cdot u^L = 0. \quad (3.5)$$

181 The Stokes drift associated with monochromatic capillary ripples propagating in the along-  
 182 wind direction  $\hat{x}$  is

$$\mathbf{u}^S(z, t) = e^{2kz} \epsilon^2 c(k) \hat{\mathbf{x}}, \quad \text{where} \quad c(k) = \sqrt{\frac{g}{k} + \gamma k} \quad (3.6)$$

is the phase speed of gravity-capillary waves in deep water with wavenumber  $k$ , gravitational acceleration  $g = 9.81 \text{ m s}^{-2}$  and surface tension  $\gamma = 7.2 \times 10^{-5} \text{ m}^3 \text{ s}^{-2}$ . In (3.6),  $\epsilon \equiv ak$  is the steepness of the capillary ripples, which is equivalent to  $\tilde{\epsilon}$  in (2.1) for monochromatic waves. In all cases considered here, the Stokes drift (3.6) is minuscule compared to the mean current  $\mathbf{u}^L \sim U$ .

We next investigate the stability of the wind-drift layer *after* ripples are generated. For this we expand the total velocity around the steady shear flow  $\tilde{U}(z)$ , such that

$$\mathbf{u}^L(y, z, t) = \tilde{U}(z) \hat{\mathbf{x}} + \mathbf{u}(y, z, t), \quad (3.7)$$

where  $\tilde{U}(z) \equiv U(z, \tilde{t})$  represents the wind-drift profile ‘frozen’ at  $\tilde{t} = 16 \text{ s}$ , and  $\mathbf{u} = (u, v, w)$  is the perturbation velocity. Inserting (3.7) into (3.4)–(3.5), introducing a streamfunction  $\psi$  with the convention  $(v, w) = (-\psi_z, \psi_y)$ , and neglecting terms that depend only on the mean flow  $U$  or  $u^S$  yields the two-dimensional system

$$u_t + \mathbf{J}(\psi, u) + \Omega \psi_y = v \Delta u, \quad (3.8)$$

$$\Delta \psi_t + \mathbf{J}(\psi, \Delta \psi) + u_z^S u_y = v \Delta^2 \psi, \quad (3.9)$$

where  $\Delta \psi = w_y - v_z$  is the  $x$ -component of the perturbation vorticity,  $\mathbf{J}(a, b) = a_y b_z - a_z b_y$  is the Jacobian operator, and  $\Omega = \tilde{U}_z - u_z^S$  is the Eulerian-mean shear — or, as we prefer, the mean, *total* cross-wind vorticity  $\nabla \times (\tilde{U} \hat{\mathbf{x}} - \mathbf{u}^S) = \Omega \hat{\mathbf{y}}$ . Equations (3.8)–(3.9) model the two-dimensional evolution of the wind-drift layer starting just after ripple generation up to the transition to three-dimensional turbulence.

We use the power method Constantinou (2015) to extract the fastest growing linear modes of (3.8)–(3.9) by iteratively integrating the wave-averaged equations (3.4)–(3.5) given (3.7) numerically from  $t = \tilde{t}$  to  $t = \tilde{t} + \Delta t$  to obtain  $\mathbf{u}$ . The numerical integrations use Oceananigans (see Ramadhan *et al.* 2020 and Wagner *et al.* 2021) with a second-order staggered volume method on a single NVidia A100 GPU in a two-dimensional domain. We use two  $y$ -periodic, vertically bounded domains with dimensions  $10 \text{ cm} \times 5 \text{ cm}$  and  $40 \text{ cm} \times 5 \text{ cm}$  to test the dependence of the results on the domain width. Because (3.4)–(3.5) are averaged over the surface ripples, the surface at  $z = 0$  is rigid and surface waves are prescribed through  $\mathbf{u}^S$  in (3.6). Impenetrable, free-slip boundary conditions are applied at the rigid top and bottom boundaries. We use  $768 \times 512$  finite volume cells in both domains, with  $0.13 \text{ mm}$  and  $0.52 \text{ mm}$  regular spacing in the horizontal and variable spacing in  $z$  with minimum vertical spacing  $\min(\Delta z) \approx 0.26 \text{ mm}$

The initial condition for the  $k^{\text{th}}$  iterate,  $\mathbf{u}^k(y, z, \tilde{t})$ , is derived by downscaling the previous iterate evaluated at  $\tilde{t} + \Delta t$ ,

$$\mathbf{u}^k|_{t=\tilde{t}} = \left[ \mathbf{u}^{k-1} \sqrt{\frac{\tilde{E}}{E^{k-1}}} \right]_{t=\tilde{t}+\Delta t}, \quad \text{where} \quad E^k \equiv \left\langle \frac{1}{2} |\mathbf{u}^k|^2 \right\rangle, \quad (3.10)$$

and  $\tilde{E}$  is the prescribed initial kinetic energy at  $t = \tilde{t}$ , and  $\langle \cdot \rangle$  denotes a volume average. The growth rate is estimated for iterate  $k$  by assuming that  $\mathbf{u}^k \propto e^{st}$ , which implies that  $|\mathbf{u}^k|^2 \propto e^{2st}$  and

$$s = \frac{1}{2\Delta t} \log \left( \frac{E^k|_{t=\tilde{t}+\Delta t}}{E^k|_{t=\tilde{t}}} \right). \quad (3.11)$$

To apply the power method we choose the integration window  $\Delta t = 0.05 \text{ s}$  with an initial perturbation kinetic energy  $\tilde{E} = 10^{-10} \text{ m}^2 \text{ s}^{-2}$ . We iterate until the growth rate estimate converges by requiring that  $(s^k - s^{k-1})/s^k < 2 \times 10^{-6}$ .

Figure 3 shows the structure of the most unstable mode for  $\epsilon = 0.1$  in a  $10 \text{ cm} \times 5 \text{ cm}$

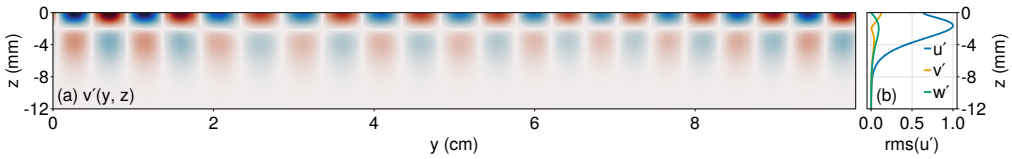


Figure 3: Numerically computed structure of the most unstable mode of the wind-drift layer at  $\tilde{t} = 16$  s (just after the inception of surface ripples) for surface ripples modeled as gravity-capillary waves with steepness  $\epsilon = ak = 0.1$  and wavenumber  $k = 2\pi/3$  cm in a  $10 \times 5$  cm domain in  $(y, z)$ . (a) Structure of the cross-wind perturbation  $v'(y, z)$  for wave steepness  $\epsilon = 0.1$  in a  $10 \times 5$  cm domain in  $(y, z)$ , (b) root-mean-square (y-averaged) perturbation profiles

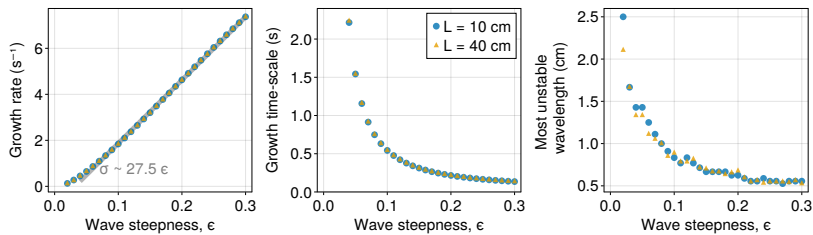


Figure 4: (a) Growth rate, (b) growth time-scale (inverse of the growth rate), and (c) wavelength of the most unstable mode of a wave-catalyzed instability of the wind-drift layer “frozen” at  $\tilde{t} = 16$  s calculated using the power method (Constantinou 2015) in two domains 10 cm and 40 cm wide.

domain in  $y, z$ . Figure 4 shows the results of a parameter sweep from  $\epsilon = 0.04$  to  $\epsilon = 0.3$ , illustrating that the wind-drift layer is susceptible to Langmuir instability for even minuscule ripple amplitudes. Figure 4a shows additionally that the growth rate  $s$  is linear in wave steepness  $\epsilon$  except at the very smallest wave amplitudes, which due to very slow growth rates are probably affected by viscous stress. Note that in the absence of waves, or alternatively for  $\epsilon = 0$ , we recover Veron & Melville (2001)’s experimental result that instability does not occur at  $\tilde{t} = 16$  s (or any other time within the duration of the experiment). Figure 4b and c show that larger wave steepnesses are associated with smaller instability wavelengths.

We emphasize that the kinetic energy source for growing perturbations is the mean shear  $\tilde{U}(z)$  and there is no energy exchange between perturbations and the surface wave field within the context of the wave-averaged equations (3.4)–(3.5). To see this, consider that (3.4)–(3.5) conserves total kinetic energy  $\int \frac{1}{2} |\mathbf{u}^L|^2 dV$  when  $v = 0$  and  $\partial_t \mathbf{u}^S = 0$  (the effects of viscous stress is negligible during the instability growth for all but the smallest wave amplitudes). This is why we characterize the shear instability as “wave-catalyzed”: while the presence of waves is necessary for instability, and while the instability growth rate is strongly affected by wave amplitude, the kinetic energy of the growing perturbation is derived solely from the mean shear.

### 3.3. Self-sharpening circulations with jets and plumes

When the wave-catalyzed shear instability reaches finite amplitude, it begins to self-sharpen, producing narrow along-wind jets and downwelling plumes. The sharpening — but still two-dimensional — plumes then transport a measurable amount of mean momentum downwards before becoming unstable to three-dimensional perturbations and thereby transitioning to fully-developed turbulence. This nonlinear sharpening and depletion of the average near-

249 surface momentum occurs between 17.5–20 s, as evidenced by the red shaded region in  
 250 figure 2b.

251 To simulate the second wave-catalyzed instability through finite amplitude and toward  
 252 transition to turbulence, we propose a simplified model based on the wave-averaged equations  
 253 (3.4)–(3.5) with two main components representing (*i*) the capillary ripples and (*ii*) the initial  
 254 condition at  $\tilde{t} = 16$  s. We model the evolving capillary ripples as steady, monochromatic  
 255 surface waves with wavenumber  $k = 2\pi/3 \text{ cm}^{-1}$ . We model the condition of the wave tank  
 256 at  $t = 16$  s with

$$257 \quad \mathbf{u}^L|_{t=\tilde{t}} = \tilde{U}(z)\hat{\mathbf{x}} + \mathbb{U}'\boldsymbol{\Xi}(x, y, z), \quad (3.12)$$

258 where  $\mathbb{U}'$  is an initial noise amplitude and  $\boldsymbol{\Xi}$  is a vector whose components are normally-  
 259 distributed random numbers with zero mean and unit variance.

260 Through experimentation, we find that the instability and transition to turbulence are only  
 261 weakly sensitive to the wavenumber  $k$ . The tuning parameters of our model are therefore (*i*)  
 262 the amplitude of the initial perturbation  $\mathbb{U}'$ , and (*ii*) the wave steepness  $\epsilon$ .

263 We also simulate the evolution of dye concentration  $\theta$  via

$$264 \quad \partial_t \theta + \mathbf{u}^L \cdot \nabla \theta = \kappa \Delta \theta, \quad (3.13)$$

265 with molecular diffusivity  $\kappa = 10^{-7} \text{ m}^2 \text{ s}^{-1}$ , the smallest we can reasonably afford computa-  
 266 tionally. (The correspondance between  $\theta$  and rhodamine is imperfect because the molecular  
 267 diffusivity of rhodamine is  $\kappa = 10^{-9} \text{ m}^2 \text{ s}^{-1}$ .) We initialize  $\theta$  with a  $\delta$ -function at the surface.

268 We integrate the wave-averaged evolution of the wind-drift layer by solving (3.4)–(3.5)  
 269 and (3.13) given (3.6) using Oceananigans in a three-dimensional, horizontally-periodic,  
 270 vertically-bounded  $10 \times 10 \times 5 \text{ cm}$  domain in  $(x, y, z)$  with 0.13 mm regular spacing in  $x, y$   
 271 and variable spacing in  $z$  with  $\min(\Delta z) \approx 0.26 \text{ mm}$ , corresponding to  $768 \times 768 \times 512$  finite  
 272 volume cells. Because (3.4)–(3.5) are averaged over surface waves, the domain contains water  
 273 only and has a flat, rigid top and bottom boundary; surface waves enter the dynamics solely  
 274 through the prescribed Stokes drift  $\mathbf{u}^S$ . Because the along-wind  $x$ -direction is periodic, our  
 275 simulations neglect large-scale along-wind variation in the ripple field and wind-drift layer.  
 276 We impose the stress (3.2) on  $\mathbf{u}^L$  at the surface and use free-slip conditions at the bottom.

277 The results of a numerical solution using the wave steepness  $\epsilon = 0.11$  and the initial  
 278 perturbation amplitude  $\mathbb{U} = 5 \text{ cm s}^{-1}$  are compared with laboratory measurements in figure 5.  
 279 (Note that with  $\mathbb{U} = 5 \text{ cm s}^{-1}$ , the random component of the initial condition hardly counts  
 280 as a “perturbation”. We discuss the significance of this shortly.) Figure 5a compares the  
 281 average surface velocity diagnosed from the simulation with the laboratory measurements  
 282 presented in figure 2b. Figure 5b plots the maximum absolute vertical velocity,  $\max |w^L|$ .  
 283 Figures 5c–l compare the simulated dye concentration on  $(y, z)$  slices with LIF measurements  
 284 of rhodamine from the laboratory experiment, showing how the simulations qualitatively  
 285 capture the observed formation, evolution, and eventual disintegration of coherent structures  
 286 during the transition to turbulence. Visualizations are shown at  $t = 18.1, 19.3, 20.0, 20.7$ , and  
 287 21.7 s. At  $t = 18.1$  s (figures 5c and d), the sharpened plumes have only just started advect  
 288 appreciable amounts of dye. At  $t = 19.3$  s (figures 5e and f), the plumes are beginning to roll  
 289 up into two-dimensional mushroom-like structures. (Note the small, unexplained discrepancy  
 290 between simulated and measured average surface velocities around  $18.1 \text{ s} < t < 19.3 \text{ s}$ .) At  
 291  $t = 20.0$  s and  $t = 20.7$  s (figures 5g, h, i, and j) three-dimensionalization and transition to  
 292 turbulence are underway. At  $t = 21.7$  s both the simulated and measured dye concentrations  
 293 appear to be mixed by three-dimensional turbulence.

294 Figure 6 illustrates the sensitivity of the wave-averaged model to amplitude of the specified  
 295 surface ripples and to the amplitude of the random initial perturbation. Figures 6a and b plot  
 296 the surface-averaged along-wind velocity  $u$  and maximum vertical velocity  $w$  for three wave

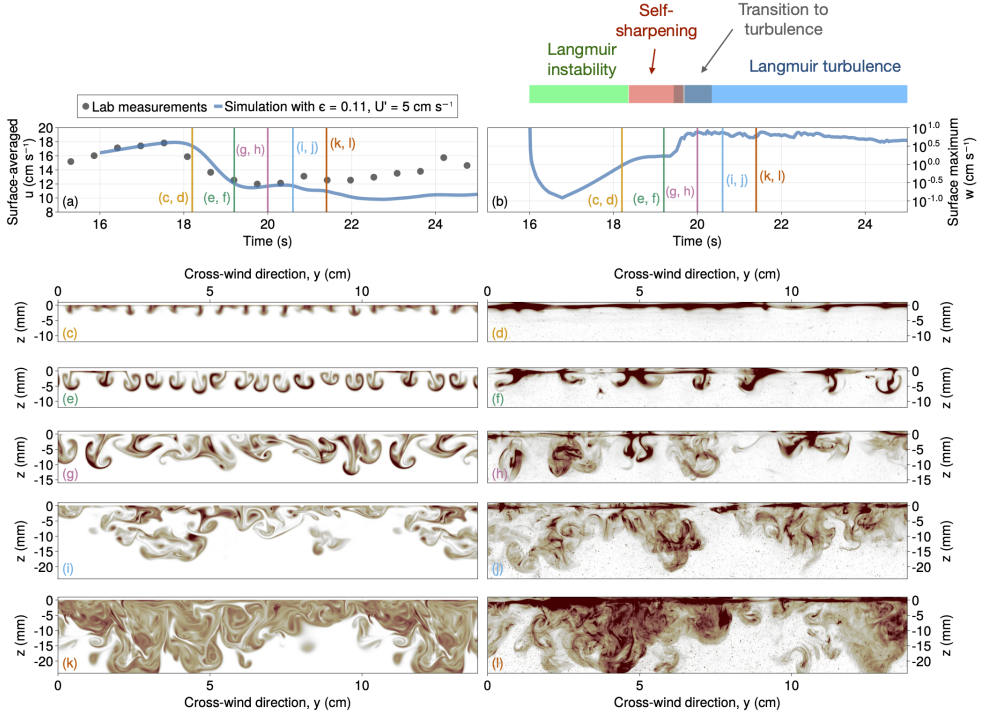


Figure 5: (a) Maximum horizontal velocity  $u$ . The grey dots are from the laboratory experiments while the blue line shows the numerical experiments. (b) Vertical velocity. (c-l) Evolution of the wind-drift layer after the emergence of capillary ripples.

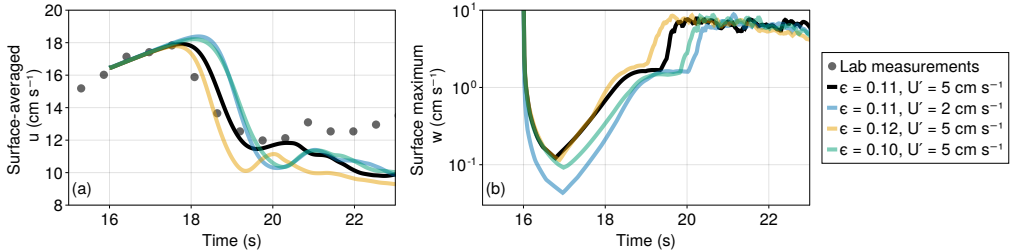


Figure 6: Sensitivity of (a) surface-averaged along-wind velocity  $u$  and (b) maximum vertical velocity to the specification of the surface wave field and initial perturbations.

amplitudes  $\epsilon = 0.10, 0.11, 0.12$  and for two initial perturbation amplitudes  $U' = 2$  and  $5 \text{ cm s}^{-1}$ . The dependence of the maximum vertical velocity is the most evocative: doubling the initial perturbation shortens the self-sharpening phase (in which the maximum vertical velocity in figure 6b flattens before increasing sharply during the transition to turbulence) by a factor of five. Of the four cases plotted in figure 6, only  $\epsilon = 0.11$  and  $U' = 5 \text{ cm s}^{-1}$  yield the satisfying agreement depicted in figure 5.

### 3.4. Langmuir turbulence

Following three-dimensionalization, momentum and dye are rapidly mixed to depth. Figure 7 visualizes (a) the  $x$ -momentum and (b) dye concentration at  $t = 23.4 \text{ s}$ , showing how the

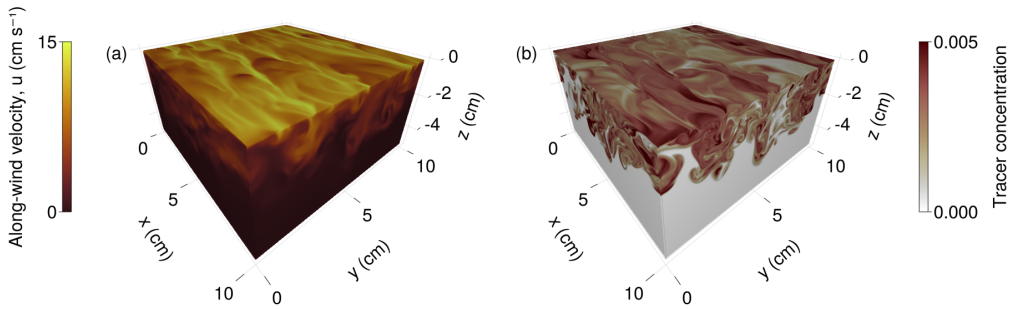


Figure 7: (a) Simulated  $x$ -momentum and (b) dye concentration at  $t = 23.4$  s, showing the streaks and jets that characterize Langmuir turbulence.

flow is organized into narrow along-wind streaks and broader downwelling regions — classic characteristics of Langmuir turbulence (Sullivan & McWilliams 2010).

In figure 8, we compare the rate which dye is mixed to depth in the simulations versus measured by LIF in the lab. Figure 8a shows the simulated horizontally-averaged tracer concentration in the depth-time ( $z, t$ ) plane, while figure 8b shows a corresponding laboratory measurements extracted from LIF measurements in the ( $y, z$ )-plane. In figures 8a and b, a light blue line shows the height  $z_{99}(t)$  defined as the level above which 99% of the *simulated* tracer concentration resides,

$$\int_{z_{99}(t)}^0 \theta \, dz = 0.99 \int_{-H}^0 \theta \, dz. \quad (3.14)$$

Using  $z_{99}(t)$  to compare the tracer mixing rates exhibited in figures 8a and b, we conclude that the simulations provided a qualitatively accurate prediction of dye mixing rates. If anything, the simulation *overpredicts* the dye mixing rate — but the data probably does not warrant more than broad qualitative conclusions.

#### 4. Discussion

This paper describes a wave-averaged model for the evolution of wind-drift layers following the inception of capillary ripples. The wave-averaged model predicts that, following ripple inception, the wind-drift layer is immediately susceptible to the growth of a second, slower, “wave-catalyzed” instability. Wave-averaged simulations show that the evolution of the wave-catalyzed instability from initial growth through transition to turbulence is sensitive not only to the amplitude of the surface ripples, but also to the amplitude of the substantial perturbations required both to seed the growth of the second-instability and to destabilize initially two-dimensional jets and plumes during the transition to turbulence.

We model the seeding and destabilizing perturbations modeled as random velocity fluctuations imposed at the time of ripple inception. However, in wind-drift layers in the laboratory or natural world, perturbations may be continuously introduced both by turbulent pressure fluctuations in the air and, perhaps more importantly, by inhomogeneities in the ripple field (see figures 3 and 15 in Veron & Melville 2001). We hypothesize that the substantial amplitude of the initial perturbations required in our simulations compensates for this missing physics.

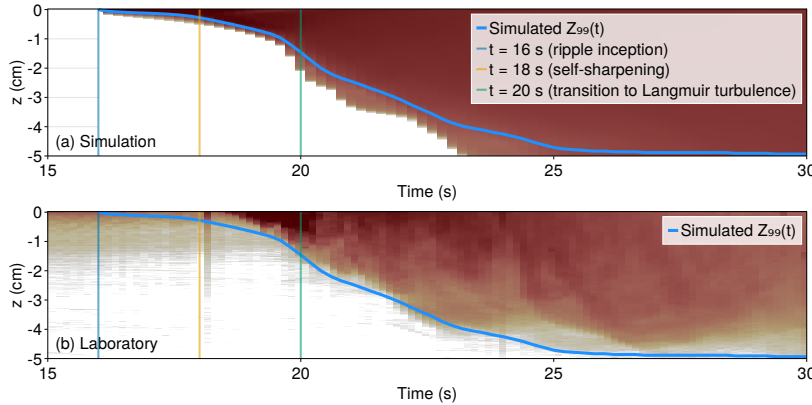


Figure 8: Visualization of mixing rates during measured and simulated wave-catalyzed instability via depth-time ( $z, t$ ) diagrams of horizontally-averaged in (a) simulations and (b) LIF-measurements. The blue lines denotes the depth above which 99% of the simulated dye resides; (b) suggests that the simulations overpredict dye mixing rates.

One of the original goals of this work was to probe the potential weaknesses of the wave-averaged Craik-Leibovich (CL) equation, which are widely used for process studies and parameterization of ocean surface boundary layer turbulence (Sullivan & McWilliams 2010). In particular, the derivation of the CL equation requires the potentially restrictive assumptions that (i) the surface wave field is nearly linear; and (ii) the timescale of the turbulence is much longer than the time scale of the waves. But despite qualitative success, firm conclusions about CL validity prove elusive due to the strong sensitivity of our results to ripple amplitude — which is evolving and two-dimensional in the laboratory experiments rather than uniform and steady, as in our model. This sensitivity, together with Veron & Melville (2001)'s observations that the ripple field is refracted and organized by turbulence in the wind-drift layer, suggests that two-way wave-turbulence coupling is important and should be described in a “predictive” theory for turbulent boundary layers affected by surface waves. Further progress requires not just theoretical advances to couple wave evolution with the CL equations, but also experiments that obtain more precise two-dimensional measurements of the evolution of the capillary ripples.

*Acknowledgements.* GLW's work is supported by the generosity of Eric and Wendy Schmidt by recommendation of the Schmidt Futures program and by the National Science Foundation grant AGS-1835576. We acknowledge stimulating discussions with Bill Young and Navid Constantinou and helpful comments from three referees. Declaration of Interests: the authors report no conflict of interest.

## REFERENCES

- BUCKLEY, MARC P & VERON, FABRICE 2017 Airflow measurements at a wavy air–water interface using piv and lif. *Experiments in Fluids* **58** (11), 161.
- CONSTANTINOU, NAVID C 2015 Formation of large-scale structures by turbulence in rotating planets. *arXiv preprint arXiv:1503.07644*.
- CRAIK, ALEX DD & LEIBOVICH, SIDNEY 1976 A rational model for Langmuir circulations. *Journal of Fluid Mechanics* **73** (3), 401–426.
- D'ASARO, ERIC A, THOMSON, J, SHCHERBINA, AY, HARCOURT, RR, CRONIN, MF, HEMER, MA & FOX-KEMPER, B 2014 Quantifying upper ocean turbulence driven by surface waves. *Geophysical Research Letters* **41** (1), 102–107.

- 364 Handler, RA, Smith, GB & Leighton, RI 2001 The thermal structure of an air–water interface at low  
365 wind speeds. *Tellus A* **53** (2), 233–244.
- 366 Harcourt, Ramsey R 2015 An improved second-moment closure model of langmuir turbulence. *Journal  
367 of Physical Oceanography* **45** (1), 84–103.
- 368 Jessup, AT, Zappa, CHRISTOPHER J & YEH, HARRY 1997 Defining and quantifying microscale wave breaking  
369 with infrared imagery. *Journal of Geophysical Research: Oceans* **102** (C10), 23145–23153.
- 370 Melville, W KENDALL, Shear, ROBERT & Veron, FABRICE 1998 Laboratory measurements of the  
371 generation and evolution of Langmuir circulations. *Journal of Fluid Mechanics* **364**, 31–58.
- 372 Ramadhan, Ali, Wagner, Gregory, Hill, Chris, Campin, Jean-Michel, Churavy, Valentin,  
373 Besard, Tim, Souza, Andre, Edelman, Alan, Ferrari, Raefaele & Marshall, John 2020  
374 Oceananigans. jl: Fast and friendly geophysical fluid dynamics on gpus. *Journal of Open Source  
375 Software* **5** (53).
- 376 Reichl, Brandon G & Li, Qing 2019 A parameterization with a constrained potential energy conversion  
377 rate of vertical mixing due to langmuir turbulence. *Journal of Physical Oceanography* **49** (11),  
378 2935–2959.
- 379 Sullivan, Peter P & McWilliams, James C 2010 Dynamics of winds and currents coupled to surface  
380 waves. *Annual Review of Fluid Mechanics* **42**, 19–42.
- 381 Sutherland, Peter & Melville, W KENDALL 2013 Field measurements and scaling of ocean surface  
382 wave-breaking statistics. *Geophysical Research Letters* **40** (12), 3074–3079.
- 383 Thorpe, SA 2004 Langmuir circulation. *Annu. Rev. Fluid Mech.* **36**, 55–79.
- 384 Vanneste, Jacques & Young, William R 2022 Stokes drift and its discontents. *Philosophical Transactions  
385 of the Royal Society A* **380** (2225), 20210032.
- 386 Veron, Fabrice & Melville, W KENDALL 1999 Pulse-to-pulse coherent doppler measurements of waves  
387 and turbulence. *Journal of Atmospheric and Oceanic Technology* **16** (11), 1580–1597.
- 388 Veron, Fabrice & Melville, W KENDALL 2001 Experiments on the stability and transition of wind-driven  
389 water surfaces. *Journal of Fluid Mechanics* **446**, 25–65.
- 390 Veron, Fabrice, Melville, W KENDALL & Lenain, Luc 2008 Wave-coherent air–sea heat flux. *Journal  
391 of physical oceanography* **38** (4), 788–802.
- 392 Wagner, Gregory L, Chini, Gregory P, Ramadhan, Ali, Gallet, Basile & Ferrari, Raefaele 2021  
393 Near-inertial waves and turbulence driven by the growth of swell. *Journal of Physical Oceanography*  
394 **51** (5), 1337–1351.
- 395 Zappa, C. J., Asher, W. E. & Jessup, A. T. 2001 Microscale wave breaking and air-water gas transfer.  
396 *Journal of Geophysical Research: Oceans* **106** (C5), 9385–9391.